Strong Exciton–Plasmon Coupling in a WS_2 Monolayer on Au Film Hybrid Structures Mediated by Liquid Ga Nanoparticles

Fu Deng, Hongfeng Liu, Lei Xu, Sheng Lan, and Andrey E. Miroshnichenko**

Realizing and manipulating strong light–matter coupling in 2D monolayer semiconductors is of paramount importance in the development of novel photonic devices. Here, it is revealed by numerical simulation that strong coupling between the excitons in a WS_2 monolayer and the surface plasmon polaritons propagating on the surface of a thin Au film can be realized when the surface plasmon polaritons are generated via the Kretschmann–Raether configuration. The use of liquid Ga nanoparticles, which exhibit broad scattering spectra in visible light, is proposed to identify the strong exciton–plasmon coupling. It is demonstrated numerically and experimentally that the exciton–plasmon coupling strength, which is manifested in Rabi splitting, can be further enhanced by the in-plane localization of the electric field provided by liquid Ga nanoparticles. Anti-crossing of the scattering spectra can be observed by tuning the angle of the incident light and Rabi splitting exceeding 120 meV can be obtained. The results open new horizons for realizing strong exciton-plasmon coupling in hybrid structures composed of monolayer semiconductors and thin metal films and pave the way for the practical applications of strong light–matter interaction in nanoscale photonic devices.

1. Introduction

Light–matter interactions including strong coupling,[1–6] Fano interference,[7–14] plasmon-induced resonance energy transfer,[15–17] plasmon-enhanced absorption and emission[18–21] have been a research hot spot of modern optics. Strong coupling regime can be accessed when the energy exchange between photons and excitons is fast enough to overcome their respective dissipation rates.[22–26] In this case, mixed states featuring part-light and part-matter are produced, leading to the spectroscopic response of the system characterized by Rabi splitting. Realizing strong light–matter coupling is of great interest due to various promising applications such as quantum manipulation,[27] ultra-fast optical switching,[28] low-threshold semiconductor lasers[29] etc.

Recent studies have successfully demonstrated strong coupling effect at the single nanoparticle level by using semiconducting transition metal dichalcogenide (TMDC) layers,[30–35] quantum dots (QDs),[36] molecules,[37–41] perovskite nanowires,[42] and TMDC nanodisks.[43] Due to the lack of efficient ways to control the excitonic orientation of molecules and QDs, the exciton-plasmon coupling relies on the change of surface plasmon resonance or the polarization of the incident light.[36,39] Different from dye molecules and QDs, the excitons in monolayer TMDCs are highly oriented in the in-plane direction and efficient dipole–dipole interaction with surface plasmon polaritons (SPPs) can be readily achieved.[30,31] More importantly, the TMDC monolayers have exceptionally high optical absorption reaching values up to 10% for MoS_2 and 15% for WS_2 at resonance.[44,45] These unique properties make them an ideal platform for realizing strong exciton–plasmon coupling, as demonstrated in a variety of systems comprising TMDC monolayers and nanophotonic resonators, including optical micro-cavities,[46,47] diffractive modes of plasmonic nanoparticle arrays,[48] and single plasmonic nanoantennas.[30–35] In practice, the spectra or energy coincidence of the resonant optical frequency and the exciton remains a technical challenge and various methods have been proposed to shift the energy of the resonator, either statically or dynamically, across that of the exciton. Remarkably, active control of strong coupling has also been demonstrated by using different methods, such as changing the nanoparticle size,[30,33,35,37] controllable and reversible switching, electro-static gating and temperature control,[30,34] controlling the refractive index of surrounding solvents,[31–33] chemical control,[31] polarization-dependent control of the incident source,[39] and the angle of incident light.[46,49]

F. Deng, H. Liu, Prof. S. Lan
Guangdong Provincial Key Laboratory of Nanophotonic Functional Materials and Devices
School of Information and Optoelectronic Science and Engineering
South China Normal University
Guangzhou 510006, China
E-mail: slan@scnu.edu.cn

F. Deng, Dr. L. Xu, Prof. A. E. Miroshnichenko
School of Engineering and Information Technology
University of New South Wales
Canberra, ACT 2600, Australia
E-mail: andrey.miroshnichenko@unsw.edu.au

DOI: 10.1002/lpor.201900420

For strong light–matter interaction, it is desirable to achieve electric field enhancement in extremely small mode volume. For this reason, nanoparticle-on-mirror systems are generally employed because TMDC layers are easily embedded in the gap region between a nanoparticle and a metal film. Recently, the strong exciton–plasmon coupling has been observed in TMDC multilayers embedded in an ultra-compact plasmonic nanocavity of nanoparticle-on-mirror geometry.[50] Unfortunately, strong coupling was not achieved in TMDC monolayers because the in-plane (or horizontally oriented) excitons in TMDC monolayers cannot be coupled to the vertical component of the electric field of the nanocavity, which has been greatly enhanced in the gap region between the metallic nanoparticle and the film. By replacing nanospheres with nanocubes, strong exciton–plasmon coupling was realized for TMDC monolayers embedded in nanoparticle-on-mirror systems owing to the significantly enhanced in-plane component of the electric field.[35] Very recently, it was suggested theoretically and numerically that strong exciton–plasmon coupling can be achieved for a WS_2 monolayer directly placed on a thin Au film when the WS_2/Au hybrid structure is excited by the SPPs generated via the Otto configuration.[49] In this case, the enhancement in the electric field is not significant, but the number of excitons involved in the interaction is large. Although this scenario is more straightforward than those reported previously, a capping layer (on top of the WS_2 monolayer) with a large dielectric constant (>9) is necessary to observe the strong coupling effect.[49]

In this work, we propose and demonstrate a novel strategy to realize and identify the strong coupling of the excitons in a WS_2 monolayer with both the propagating SPPs and the localized surface plasmon resonances (LSPRs). Our numerical simulations reveal that the strong coupling between the excitons in a WS_2 monolayer and SPPs can be realized at room temperature via the Kretschmann–Raether (K–R) configuration. Then, we confirm numerically and experimentally that the exciton–plasmon coupling in the WS_2/Au hybrid structure can be revealed and enhanced by using liquid Ga nanoparticles which exhibit broad scattering spectra in visible light. Finally, we show a stronger exciton–plasmon coupling realized in the nanoparticle-on-mirror system (with a Rabi splitting exceeding ≈120 meV) and demonstrate the engineering of the exciton–plasmon coupling strength by merely varying the angle of the incident light. Our findings are helpful for investigating strong light-matter interaction and useful for designing nanoscale photonic devices.

2. Results and Discussion

We first examined the coupling of the excitons in a WS_2 monolayer placed on an Au/SiO_2 substrate with the SPPs generated on the surface of the Au film (50 nm) via the K–R configuration, as schematically shown in **Figure** 1a. It is well known that the SPPs can only be excited by TM-polarized light and the resonant wavelength of the SPPs, which is manifested as a dip in the reflection spectrum, exhibits a strong dependence on the angle of the incident light, as shown in Figure 1b. Therefore, one can shift the energy (or wavelength) of the SPPs by merely varying the incidence angle. The coupling between the excitons and the SPPs is expected to occur once the two resonances are spectrally overlapped. Figure 1c shows the 2D plot of the reflectance as functions of the incidence angle and wavelength calculated for the WS_2/Au hybrid structure. Surprisingly, an anti-crossing is observed at an incidence angle of about 45°, which is also shown in Figure 1d. This behavior is entirely different from the excitation of the WS_2/Au hybrid structure via the Otto configuration[49] where a capping layer with a dielectric constant larger than nine is needed in order to observe a pronounced anti-crossing. By employing the K–R configuration rather than the Otto one, the in-plane component of the electric field is enhanced to some extent, making it possible to realize the strong exciton–plasmon coupling without using any capping layer on the WS_2 monolayer (more details can be found in Figure S3, Supporting Information).

The exciton–plasmon coupling in the WS_2/Au hybrid structure can be described by using the coupled harmonic oscillator model.[39] In the strong coupling regime, the respective contributions of the exciton and plasmon components can be calculated as follows[25,30,31,35]

$$\begin{pmatrix} E_{pl} - \frac{i\hbar\gamma_{pl}}{2} & g \\ g & E_{ex} - \frac{i\hbar\gamma_{ex}}{2} \end{pmatrix} \begin{pmatrix} \alpha \\ \beta \end{pmatrix} = E_{\pm} \begin{pmatrix} \alpha \\ \beta \end{pmatrix} \quad (1)$$

where E_{pl} and E_{ex} are the energies of the plasmons in the absence of WS_2 and the X_0 excitons of WS_2, respectively. γ_{pl} and γ_{ex} are the dissipation rates of the two oscillators. g is the coupling strength, and $E_{\pm}$ are the eigen-energies of the hybrid states. The parameters α and β are the eigenvector components (Hopfield coefficients) and satisfy $|\alpha|^2 + |\beta|^2 = 1$. By considering the detuning, the eigenvalues can be obtained as

$$E_{\pm} = \frac{E_{pl} + E_{ex}}{2} \pm \frac{\sqrt{4g^2 + \left(\delta - \frac{i}{2}(\gamma_{pl} - \gamma_{ex})\right)^2}}{2} \quad (2)$$

with $\delta = E_{pl} - E_{ex}$ the energy difference between the plasmons and the excitons. The Rabi splitting energy, $\hbar\Omega = \sqrt{4g^2 - \frac{(\gamma_{pl} - \gamma_{ex})}{4}}$, can be obtained when $E_{pl} = E_{ex}$.

Since γ_{pl} can be extracted from the reflection spectra and γ_{ex} is derived to be ≈33 meV based on the algorithm proposed previously,[33,34,45] we can fit the results shown in Figure 1c using the coupled harmonic oscillator model and extract the Rabi splitting energy as ≈89.8 meV. It should be emphasized that there are two criteria for strong coupling. The first one is the appearance of anti-crossing behavior in the energy diagram, which has been observed in Figure 1d. The second one is that the energy splitting should fulfill the condition $\hbar\Omega > \frac{\gamma_{pl} - \gamma_{ex}}{2}$ or $\hbar\Omega > \frac{\gamma_{pl} + \gamma_{ex}}{2}$,[39,40] where γ_{pl} and γ_{ex} represent the line widths of the optical mode and the exciton transition, respectively. In our case, the criterion of $\hbar\Omega > \frac{\gamma_{pl} - \gamma_{ex}}{2}$ is fulfilled, implying that the coupling between the excitons in the WS_2 monolayer and the SPPs generated on the surface of the Au film via the K–R configuration enters the strong coupling regime.

To gain a deep insight into the strong exciton–plasmon coupling achieved in the WS_2/Au hybrid structure, we calculated the electric field distributions of the SPPs without and with the WS_2 monolayer, as shown in **Figure** 2. The generation of the SPPs is

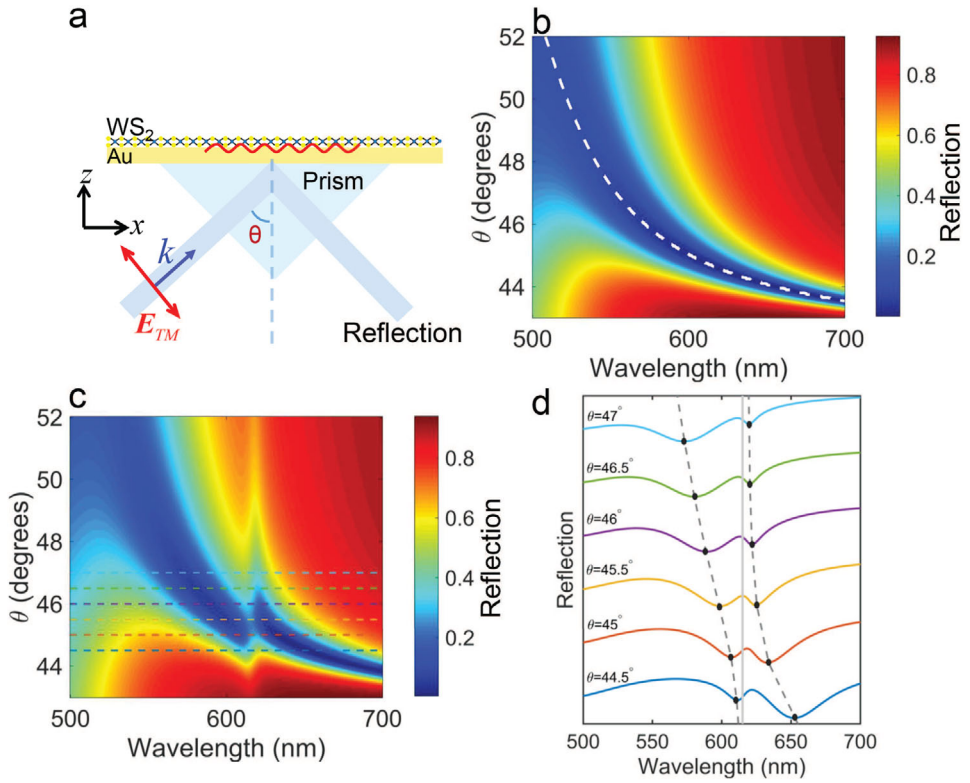

Figure 1. a) Schematic showing a WS_2 monolayer placed on a 50-nm-thick Au film and excited by the propagating SPPs generated via the K-R configuration. θ represents the angle of the incident light. Two-dimensional plot of the reflectance as functions of the incidence angle and wavelength without b) and with c) the WS_2 monolayer. The white dashed line in b) represents the resonant wavelength of SPPs generated at different angles. d) Reflection spectra of the WS_2/Au hybrid structure calculated at different incidence angles (dashed lines in c)). The black dashed curves are the fitting results of the reflection dips.

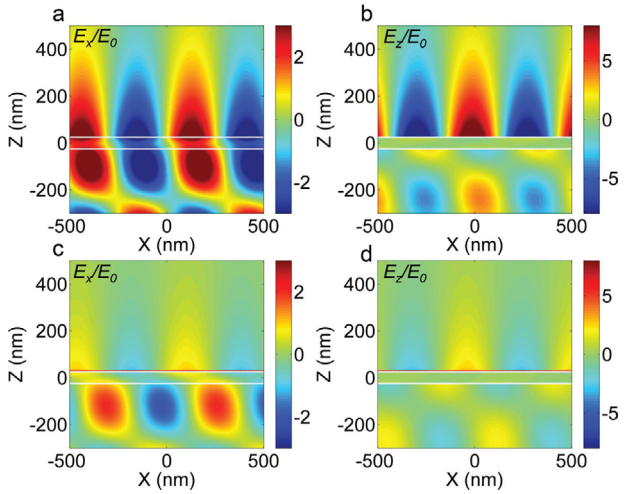

Figure 2. Electric field distributions calculated for the Au film and the WS_2/Au hybrid structure at an incidence angle of $\theta = 46°$ at the reflection dip without WS_2 [(a) and (b)] and at the coupled wavelength of the case with WS_2 [(c) and (d)]. Panels (a) and (c) represent the *x*-component (E_x) of the electric field without and with the WS_2 monolayer, respectively. Panels (b) and (d) represent the *z*-component (E_z) of the electric field without and with WS_2 monolayer, respectively. In each case, the Au film is denoted by two white lines. The WS_2 monolayer is denoted by red lines in (c) and (d).

manifested in the exponential decay of the electric field in the *z*-direction. It is noticed that the enhancement factors for the *x* and *z* components of the electric field are ≈3 and ≈10 in the absence of the WS_2 monolayer. Owing to the propagating characteristic of the SPPs, the number of horizontally-oriented excitons in the WS_2 monolayer interacting with the SPPs is quite large. For this reason, the strong exciton-plasmon can be achieved although the enhancement factor for the in-plane electric field (the *x* component) is only ≈3. After adding the WS_2 monolayer, it can be seen that both the *x* and *z* components of the electric field are greatly attenuated because the coupling of the incident light into the SPPs is dramatically reduced due to the mode splitting induced by the strong exciton-plasmon coupling. In this case, the intensity of the reflected light is increased, as shown in Figure 1d.

To verify experimentally the strong exciton-plasmon coupling realized in the WS_2/Au hybrid structure, one needs to measure the reflection spectra at different incidence angles. In our experimental setup, we employed a collimated white light with a diameter of ≈1.0 cm to excite the SPPs on the surface of the Au film. In this case, the spectra of the reflected light with increasing incidence angle can be measured because of the large area of the Au film (see Figure S4, Supporting Information). However, it is a technical challenge to measure the spectra of the reflected light in the presence of the WS_2 monolayer because of the difficulties in generating a collimated white light with a diameter smaller than the size of the WS_2 monolayer (≈100 μm) and locating it

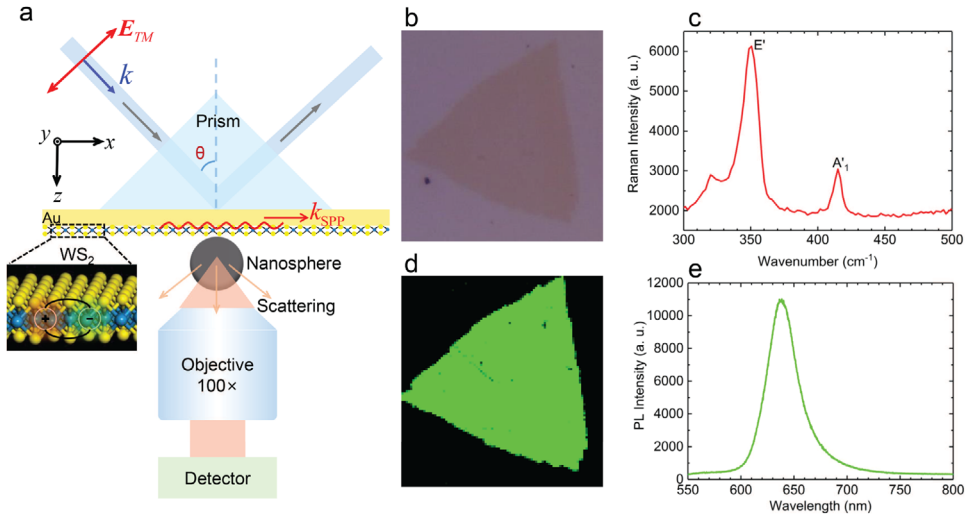

Figure 3. a) Schematic showing the plasmonic nanocavity formed by a Ga nanoparticle placed on the Au film with an embedded WS_2 monolayer. The nanocavity is excited by the SPPs generated via the K-R configuration. The angle of the incident light is θ. b) Optical image of the WS_2 monolayer placed on the Au film. c) Raman scattering spectrum measured for the WS_2 monolayer. d) 2D mapping of the Raman signal of the WS_2 monolayer at ≈414 cm^{-1}. e) PL spectrum of the WS_2 monolayer.

accurately on the WS_2 monolayer. As an alternative, one can introduce a nanoparticle on top of the WS_2 monolayer and extract the information of strong coupling from the scattering spectra of the nanoparticle measured at different incidence angles. It is required, however, that the nanoparticle exhibits a broad scattering spectrum spanning the visible to the near-infrared spectral range so that the spectrum of the SPPs can be accurately reproduced, similar to the spectrum of the reflected light which gives the spectrum of the SPPs directly. In practice, we can choose either dielectric nanoparticles (e.g., polystyrene (PS) nanospheres or silicon (Si) nanospheres) or metallic nanoparticles (e.g., Au nanospheres) as the scatters for the SPPs. It has been confirmed that PS nanospheres with diameters of ≈200 nm can really be used to scatter the SPPs efficiently in the forward direction. At each angle, the peak and linewidth of the scattering spectrum, which reflect the resonant wavelength and dissipation rate of the SPPs, are quite similar to those observed in the reflection spectrum. Owing to the small refractive index of PS, the electric field enhancement achieved in the gap region between the PS nanosphere and Au film is weaker than that obtained by using metallic nanoparticles and stronger exciton–plasmon coupling is not expected (details are shown in Figure S5, Supporting Information). For dielectric nanoparticles with high refractive indices, such as Si nanoparticles, a stronger enhancement in the electric field can be realized. However, the simultaneous excitation of the electric dipole and magnetic dipole in a Si nanoparticle excited by the SPPs leads to the formation of a Fano resonance in the scattering spectrum, making it difficult to reveal the Rabi splitting induced by the strong exciton–plasmon coupling. Therefore, it is preferred to use a metallic nanoparticle to form a plasmonic cavity in combination with the Au film, which can be employed to enhance the exciton–plasmon interaction.

One of the advantages of using metallic nanoparticles, such as Au nanospheres, is the enhancement in the in-plane component of the electric field through the strong localization of the electric field in the gap region between the metallic nanoparticle and the Au film. In this case, LSPRs rather than propagating SPPs are generated, and the interaction of the plasmonic mode with the excitons in the WS_2 monolayer will be significantly enhanced. At first glance, it seems that Au nanoparticles are the best choice for constructing plasmonic nanocavities with the Au film. Previously, Au nanorods placed on a WS_2 monolayer have been successfully used to demonstrate the strong exciton-plasmon coupling.[30] However, the small scattering cross sections of small Au nanoparticles lead to weak scattering light and unsatisfied signal-to-noise ratio. For large Au nanoparticles, the appearances of higher-order plasmon modes may affect the observation of the strong coupling in the scattering spectra and hinder the accurate extraction of the Rabi splitting energy.[51] Very recently, we have successfully fabricated liquid Ga nanospheres with different diameters in water by using femtosecond laser ablation.[52] It was found that liquid Ga nanoparticles exhibit broad scattering spectra spanning the visible light to the near-infrared spectral range, quite similar to polymer nanoparticles. Specifically, the high-order plasmon modes in large liquid Ga nanoparticles also possess broad line widths. This unique feature makes it possible to use large liquid Ga nanoparticles to enhance the signal-to-noise ratio and to distinguish the energy splitting appearing the scattering spectra. On the other hand, liquid Ga nanoparticles can be used to create plasmonic nanocavities by placing on the Au film with a dramatically enhanced electric field, boosting exciton–plasmon coupling. For these reasons, liquid Ga nanoparticles were used in this work to demonstrate the strong exciton–plasmon coupling achieved in the WS_2/Au hybrid structure.

In our experiments, liquid Ga nanoparticles were randomly distributed on the WS_2 monolayer by using drop-casting, creating plasmonic nanocavities with the Au film. The LSPRs of the plasmonic nanocavities can be easily tuned by simply changing the angle of the incident light, as schematically shown in **Figure** 3a. The optical image of the WS_2 monolayer is shown in Figure 3b. The crystalline structure of the WS_2 monolayer was

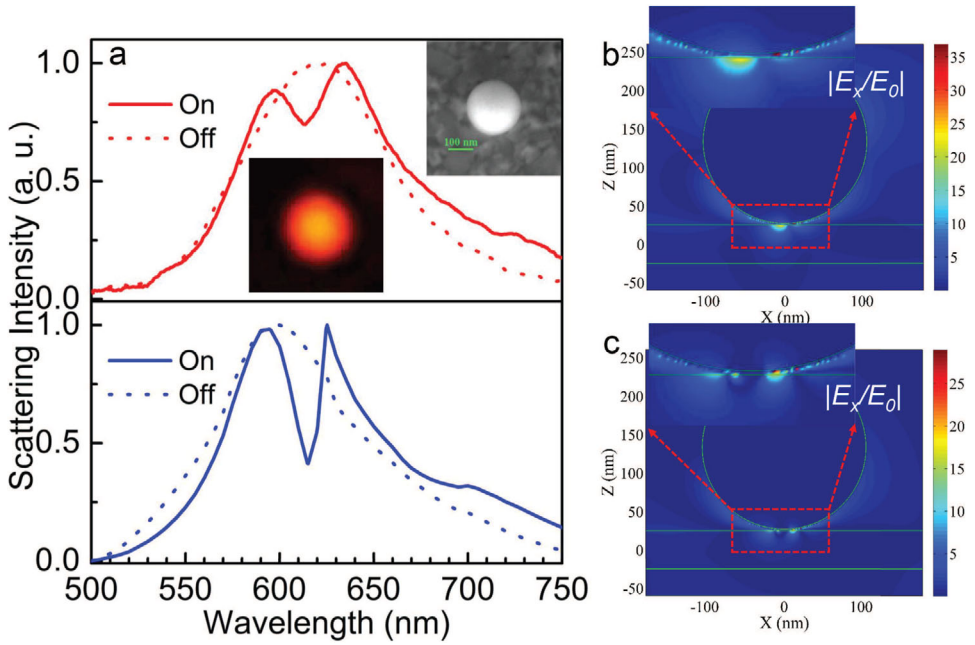

Figure 4. a) Scattering spectrum measured for a Ga nanoparticle (with a diameter of ≈212.6 nm) placed on the WS_2/Au hybrid structure (solid curve) at an incidence angle of 46° (upper panel). Also shown is the scattering spectrum measured for another Ga nanoparticle with a similar diameter placed on the Au film (dashed curve). The calculated scattering spectra with (solid curve) and without (dashed curve) the WS_2 monolayer are provided for comparison (lower panel). The SEM image of the Ga nanoparticle and the CCD image of the scattering light are shown as insets. Panels b) and c) show the distributions of the *x*-component of the electric field (E_x) of the plasmonic nanocavity without and with the WS_2 monolayer, respectively. Green lines denote the outlines of the Ga nanoparticle and the Au film.

confirmed by Raman scattering measurements, as shown in Figure 3c. Two main peaks centered at ≈350 and ≈414 cm^{-1} were observed in the Raman scattering spectrum, corresponding to the out-of-plane E′ and the in-plane A'_1 modes of the WS_2 monolayer, respectively.[53,54] Besides, the photoluminescence (PL) spectrum of the WS_2 monolayer measured at room temperature shows a single intense peak centred at ≈630 nm, in good agreement with the exciton emission reported for the WS_2 monolayer grown by using chemical vapour deposition.[55,56] Therefore, we confirmed by Raman scattering and PL measurements the monolayer nature of the WS_2 flake used in this work with a thickness of ≈1 nm.[57,58] In **Figure** 4a, we present the scattering spectra measured and calculated for a Ga nanoparticle with a diameter of ≈212.6 nm, which is excited by using a TM-polarized light at an incidence angle of 46°. The CCD image of the WS_2/Au hybrid structure excited by the SPPs can be found in Figure S6, Supporting Information. The SEM image of the Ga nanoparticle and the CCD image of the scattering light are shown in the insets. In the numerical simulations, we were able to calculate the scattering spectrum of the Ga nanoparticle in the absence of the WS_2 monolayer. In this case, the scattering spectrum appeared as broadband (see the dashed curve). By adding the WS_2 monolayer, a mode splitting was observed. The experimental observations also confirmed this behaviour. With the help of SEM observation, we were able to find another Ga nanoparticle on the Au film, whose diameter is close to that of the Ga nanoparticle located on the WS_2 monolayer, and measure its scattering spectrum (see the dashed curve). It is noticed that the broad scattering spectrum in the absence of the WS_2 monolayer splits into two modes which ambiguously verifies that the mode splitting is indeed induced by the coupling of the excitons in the WS_2 monolayer with the plasmons supported by the nanocavity. It should be emphasized that the excitation of the LSPRs of the plasmonic nanocavity by using the K–R configuration plays a crucial role for observing the mode splitting or strong coupling because this phenomenon was not observed when measuring the backward scattering spectrum of the Ga nanoparticle. In the later case, the field enhancement of E_x is only 4.0 (see Figure S7, Supporting Information), which is not sufficient for observing strong exciton-plasmon coupling.

The strong exciton–plasmon coupling realized in the plasmonic nanocavity is attributed to the enhanced in-plane component of the electric field due to the introduction of the Ga nanoparticle. In Figure 4b,c, we show the distributions of the *x*-component (in-plane component) of the electric field inside the nanocavity without and with the WS_2 monolayer. It can be seen that an enhancement factor as large as ≈35 can be achieved for the *x*-component of the electric field when the nanocavity is excited by the SPPs generated via the K-R configuration. This value is one order of magnitude larger than that obtained in the absence of the Ga nanoparticle (Figure 2), which boost the interaction between the plasmonic cavity and the WS_2 monolayer significantly. It is also noticed that the energy exchange between the plasmonic nanocavity and the WS_2 monolayer in the strong coupling regime leads to the modification of the electric field distribution.

In **Figure** 5, we present the scattering spectra of the plasmonic cavity measured at different incidence angles. Remarkably, the exciton–plasmon coupling can be dynamically tuned

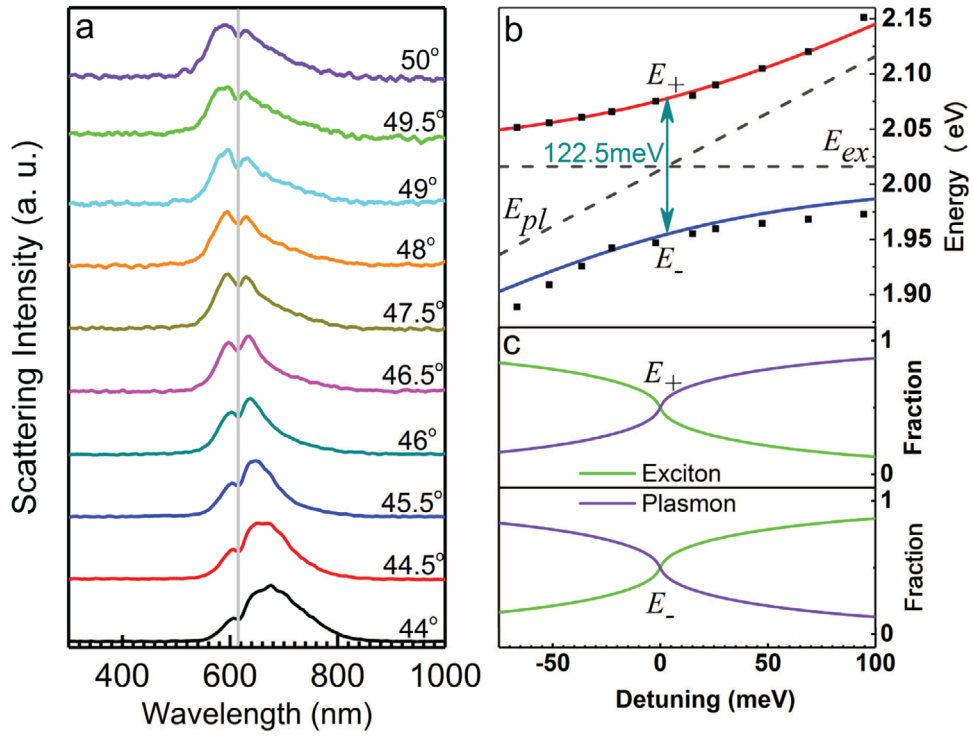

Figure 5. a) Evolution of the scattering spectrum of the plasmonic nanocavity with increasing incidence angle. b) Energy dependency of the hybrid modes on the energy detuning. The black cubes are the experimental results, while the solid coloured curves are the fitting results based on the coupled harmonic oscillator model. c) Plasmon and exciton fractions calculated for the upper and lower plexciton branches of the plasmonic nanocavity with the embedded WS_2 monolayer, respectively.

by simply varying the angle of the incident light, providing an effective and convenient way to engineer the coupling strength. The anti-crossing behavior, which is a typical characteristic of the strong coupling between the plasmonic cavity and the exciton transition,[25,26] can be identified in the evolution of the scattering spectrum with increasing the incidence angle (Figure 5a). The dependencies of the energies of the two hybrid modes on the detuning energy between the exciton and plasmon are shown in Figure 5b. The theoretical calculations based on the coupled harmonic oscillator model are also provided for comparison. The experimental observations agree well with the theoretical predictions. The Rabi splitting, which is defined as the energy difference between the high- and low-energy hybrid modes at zero detunings, is derived to be ≈122.5 meV. To the best of our knowledge, the Rabi splitting observed in our plasmonic nanocavities composed of Ga nanoparticles and the Au film is comparable or even larger than those reported in other nanoparticle-on-WS_2 monolayer systems,[30–35] indicating the effectiveness of using Ga nanoparticles in combination with Au film to create plasmonic nanocavities with the dramatically enhanced in-plane electric field.

From the above experimental results, γ_{pl} is derived to be ≈258 meV from the scattering spectra without WS_2 monolayer (see Figure S8, Supporting Information). In addition, γ_{ex} is obtained as ≈33 meV from the algorithm proposed previously.[33,34,45] Hence, the mode splitting energy observed in our experiments fulfills the criterion of $\hbar\Omega > \frac{\gamma_{pl}-\gamma_{ex}}{2}$. It indicates undoubtedly that the coupling between the plasmonic cavity and the WS_2 monolayer enters the strong coupling regime. Therefore, the plasmonic (upper plexciton branches) and exciton (lower plexciton branches) fractions for the high- and low-energy hybrid modes of the nanocavity with an embedded WS_2 monolayer can be obtained, as shown in Figure 5c. It is also found that the plasmon (exciton) constituent dominates upper (lower) plexciton branches for a large incidence angle and the situation reverses for a small incidence angle. In order to confirm that the observed strong coupling does not arise from the interaction between the plasmon modes in large liquid Ga nanoparticles and WS_2 monolayer, we also measured the scattering spectra of Ga nanoparticles in the absence of the Au film (see Figure S9, Supporting Information). In this case, the linewidth of the scattering spectrum of the Ga nanoparticle, which reflects the damping rate of the plasmons, is broadened dramatically. As a result, the criterion for strong coupling is no longer fulfilled because of the large damping rate of the plasmons, indicating that only weak coupling is obtained in the absence of the Au film.

3. Conclusions

In summary, we have investigated the exciton-plasmon coupling in a WS_2/Au hybrid structure and revealed numerically that strong coupling could be realized by using the SPPs generated via the K–R configuration. The anti-crossing behavior can be observed in the evolution of the reflection spectrum with increasing incidence angle, and the Rabi splitting can be derived

based on the coupled harmonic oscillator model. We showed both numerically and experimentally that the exciton–plasmon coupling can be further improved by creating compact plasmonic nanocavities by using liquid Ga nanoparticles, which exhibit broad scattering spectra in the visible to the near-infrared spectral range. It was found that the in-plane electric field is enhanced by one order of magnitude due to the introduction of Ga nanoparticles. Rabi splitting as large as ≈120 meV was observed at room temperature and the coupling strength can be dynamically and conveniently adjusted by only varying the angle of the incident light. Our findings open new horizons for enhancing and engineering the excition-plasmon coupling and indicate the potential applications of such plasmonic cavities in the construction of novel plasmonic devices operating at room temperature.

Experimental Section

Sample Preparation: The WS_2 monolayer used in this work was synthesized on a silicon substrate via chemical vapor deposition (CVD) method and then transferred to an Au/SiO_2 substrate with a 50-nm-thick Au film. Ga nanoparticles with different diameters were fabricated by using femtosecond laser ablation.[52] A solid state Ga film immersed in deionized water was used as the target. The 800-nm femtosecond laser pulses (Legend, Coherent) with a duration of 100 fs, a repetition rate of 1 kHz, and an average power of 1 mW were employed to ablate the Ga film. The fabricated Ga nanoparticles are composed of liquid cores (Ga) and solid shells (Ga_2O_3).[59] The aqueous solution of Ga nanoparticles was dropped and dried on the WS_2 monolayer supported by the Au/SiO_2 substrate, obtaining plamonic nanocavities with an embedded WS_2 monolayer.

Scattering Imaging and Spectroscopy: The scattering spectra of the plasmonic nanocavities with an embedded WS_2 monolayer were recorded by using a dark-field microscope (Axio Observer A1, Zeiss) quipped with a spectrometer (SR-500i-B1, Andor) and a color charge coupled device (CCD) (DS-Ri2, Nikon). The SPPs were generated via the K-R configuration and a 100× objective with NA = 0.80 was employed to collect the scattered light. The scattering spectra were corrected by first subtracting the background spectra taken from the adjacent regions and then divided by using the calibrated response curve of the entire optical system. The integration time for the spectrum measurements was chosen to be 1 s.

Characterization of WS_2 Monolayer: The morphology of a WS_2 monolayer was examined by using scanning electron microscope (SEM) (Ultra55, Zeiss) (see Figure S1, Supporting Information). The photoluminescence and Raman spectra of the WS_2 monolayer were measured by using a 532 nm laser and a Renishaw inVia Reflex system, respectively. The laser power used for the PL and Raman spectra measurements was 1 mW.

Numerical Simulations: In this work, the numerical simulations were performed by using the finite-difference time-domain (FDTD) method (see Figure S2, Supporting Information for details). The dielectric function of Au was taken from the experimental data[60] while those for WS_2, Ga, and Ga_2O_3 were taken from previous literature.[45,60,61] The exciton energy in WS_2 monolayer is 2.02 eV. The refractive indices of the prism and the surrounding media were chosen to be 1.5 and 1.0, respectively. In the calculation of the scattering spectra, the diameter of the Ga nanoparticle was chosen to be 212.6 nm while the thickness of the WS_2 monolayer was chosen to be 1.0 nm. In addition, the angle of the incident light (TM-polarized) was set to be 46°. A mesh size as small as 0.5 nm was used in the the gap region between the nanoparticle and the film to ensure the convergence of the numerical simulations and the achievement of accurate results.

Supporting Information

Supporting Information is available from the Wiley Online Library or from the author.

Acknowledgements

This work was supported by National Key Research and Development Program of China (Grant No. 2016YFA0201002), National Nature and Science Foundation of China (Grant Nos. 11674110 and 11874020), Natural Science Foundation of Guangdong Province, China (Grant No. 2016A030308010), Innovation Project of Graduate School of South China Normal University (Grant No. 2018LKXM041). F.D. acknowledges the Top Graduate Student Study Abroad Project of South China Normal University. A.E.M. acknowledges the support from the Australian Research Council and UNSW Scientia Fellowship.

Conflict of Interest

The authors declare no conflict of interest.

Keywords

2D material, liquid Ga nanoparticle, rabi splitting, strong coupling

Received: December 2, 2019
Revised: January 19, 2020
Published online: March 5, 2020

[1] J. Bellessa, C. Bonnand, J. C. Plenet, J. Mugnier, *Phys. Rev. Lett.* **2004**, *93*, 036404.
[2] G. A. Wurtz, P. R. Evans, W. Hendren, R. Atkinson, W. Dickson, R. J. Pollard, A. V. Zayats, W. Harrison, C. Bower, *Nano Lett.* **2007**, *7*, 1297.
[3] E.-M. Roller, C. Argyropoulos, A. Högele, T. Liedl, M. Pilo-Pais, *Nano Lett.* **2016**, *16*, 5962.
[4] S. Balci, C. Kocabas, S. Ates, E. Karademir, O. Salihoglu, A. Aydinli, *Phys. Rev. B* **2012**, *86*, 235402.
[5] W. H. Ni, T. Ambjornsson, S. P. Apell, H. J. Chen, J. F. Wang, *Nano Lett.* **2009**, *10*, 77.
[6] L. H. Lin, M. S. Wang, X. L. Wei, X. L. Peng, C. Xie, Y. B. Zheng, *Nano Lett.* **2016**, *16*, 7655.
[7] M. Frimmer, T. Coenen, A. F. Koenderink, *Phys. Rev. Lett.* **2012**, *108*, 077404.
[8] W. Zhang, A. O. Govorov, *Phys. Rev. B* **2011**, *84*, 081405.
[9] A. Ridolfo, O. Di Stefano, N. Fina, R. Saija, S. Savasta, *Phys. Rev. Lett.* **2010**, *105*, 263601.
[10] A. E. Miroshnichenko, S. Flach, Y. S. Kivshar, *Rev. Mod. Phys.* **2010**, *82*, 2257.
[11] B. Luk'yanchuk, N. I. Zheludev, S. A. Maier, N. J. Halas, P. Nordlander, H. Giessen, C. T. Chong, *Nat. Mater.* **2010**, *9*, 707.
[12] J. B. Lassiter, H. Sobhani, J. A. Fan, J. Kundu, F. Capasso, P. Nordlander, N. J. Halas, *Nano Lett.* **2010**, *10*, 3184.
[13] R. R. Frontiera, N. L. Gruenke, R. P. Van Duyne, *Nano Lett.* **2012**, *12*, 5989.
[14] X. N. Liu, N. Kongsuwan, X. G. Li, D. X. Zhao, Z. M Wu, O. Hess, X. H. Zhang, *J. Phys. Chem. Lett.* **2019**, *10*, 7594.
[15] J. T. Li, S. K. Cushing, F. Meng, T. R. Senty, A. D. Bristow, N. Q. Wu, *Nat. Photonics* **2015**, *9*, 601.
[16] G. L. Liu, Y.-T. Long, Y. Choi, T. Kang, L. P. Lee, *Nat. Methods* **2007**, *4*, 1015.
[17] M. S. Wang, B. B. Rajeeva, L. Scarabelli, E. P. Perillo, A. K. Dunn, L. M. Liz-Marzán, Y. B. Zheng, *The J. Phys. Chem. C* **2016**, *120*, 14820.
[18] T. Ming, L. Zhao, Z. Yang, H. J. Chen, L. D. Sun, J. F. Wang, C. H. Yan, *Nano Lett.* **2009**, *9*, 3896.

[19] M. S. Wang, G. Hartmann, Z. L. Wu, L. Scarabelli, B. B. Rajeeva, J. W. Jarrett, E. P. Perillo, A. K. Dunn, L. M. Liz-Marzán, G. S. Hwang, Y. B. Zheng, *Small* **2017**, *13*, 1701763.
[20] G. M. Akselrod, C. Argyropoulos, T. B. Hoang, C. Ciracì, C. Fang, J. N. Huang, D. R. Smith, M. H. Mikkelsen, *Nat. Photonics* **2014**, *8*, 835.
[21] Y. L. Wang, C. Li, G. Y. Duan, L. L. Wang, L. Yu, *Adv. Opt. Mater.* **2019**, *7*, 1801362.
[22] J. M. Raimond, M. Brune, S. Haroche, *Rev. Mod. Phys.* **2001**, *73*, 565.
[23] G. Khitrova, H. M. Gibbs, M. Kira, S. W. Koch, A. Scherer, *Nat. Phys.* **2006**, *2*, 81.
[24] S. Smolka, W. Wuester, F. Haupt, S. Faelt, W. Wegscheider, A. Imamoglue, *Science* **2014**, *346*, 332.
[25] P. Törmä, W. L. Barnes, *Reports on Prog. Phys.* **2014**, *78*, 013901.
[26] D. G. Baranov, M. Wersäll, J. Cuadra, T. J. Antosiewicz, T. Shegai, *ACS Photonics* **2017**, *5*, 24.
[27] M. A. Sillanpää, J. I. Park, R. W. Simmonds, *Nature* **2007**, *449*, 438.
[28] W. L. Chen, K. M. Beck, R. Bücker, M. Gullans, M. D. Lukin, H. Tanji-Suzuki, V. Vuletic, *Science* **2013**, *341*, 768.
[29] S. K. Cohen, S. R. Forrest, *Nat. Photonics* **2010**, *4*, 371.
[30] J. X. Wen, H. Wang, W. L. Wang, Z. X. Deng, C. Zhuang, Y. Zhang, F. Liu, J. C. She, J. Chen, H. J. Chen, S. Z. Deng, N. S. Xu, *Nano Lett.* **2017**, *17*, 4689.
[31] D. Zheng, S. P. Zhang, Q. Deng, M. Kang, P. Nordlander, H. X. Xu, *Nano Lett.* **2017**, *17*, 3809.
[32] M. S. Wang, A. Krasnok, T. Y. Zhang, L. Scarabelli, H. Liu, Z. L. Wu, L. M. Liz-Marzán, M. Terrones, A. Alù, Y. B. Zheng, *Nano Lett.* **2017**, *17*, 4689.
[33] S. Lepeshov, M. S. Wang, A. Krasnok, O. Kotov, T. Y. Zhang, H. Liu, T. Z. Jiang, B. Korgel, M. Terrones, Y. B. Zheng, A. Alù, *ACS Appl. Mater. & Interfaces* **2018**, *10*, 16690.
[34] J. Cuadra, D. G. Baranov, M. Wersäll, R. Verre, T. J. Antosiewicz, T. Shegai, *Nano Lett.* **2018**, *18*, 1777.
[35] X. B. Han, K. Wang, X. Y. Xing, M. Y. Wang, P. X. Lu, *ACS Photonics* **2018**, *5*, 3970.
[36] K. Santhosh, O. Bitton, L. Chuntonov, G. Haran, *Nat. Commun.* **2016**, *7*, 11823.
[37] R. Chikkaraddy, B. De Nijs, F. Benz, S. J. Barrow, O. A. Scherman, E. Rosta, A. Demetriadou, P. Fox, O. Hess, J. J. Baumberg, *Nature* **2016**, *535*, 127.
[38] R. M. Liu, Z. K. Zhou, Y. C. Yu, T. W. Zhang, H. Wang, G. H. Liu, Y. M. Wei, H. J. Chen, X. H. Wang, *Phys. Rev. Lett.* **2017**, *118*, 237401.
[39] A. E. Schlather, N. Large, A. S. Urban, P. Nordlander, N. J. Halas, *Nano Lett.* **2013**, *13*, 3281.
[40] G. Zengin, M. Wersäll, S. Nilsson, T. J. Antosiewicz, M. Käll, T. Shegai, *Phys. Rev. Lett.* **2015**, *114*, 157401.
[41] M. Wersäll, J. Cuadra, T. J. Antosiewicz, S. Balci, T. Shegai, *Nano Lett.* **2017**, *17*, 551.
[42] Q. Y. Shang, S. Zhang, Z. Liu, J. Chen, P. F. Yang, C. Li, W. Li, Y. F. Zhang, Q. H. Xiong, X. F. Liu, Q. Zhang, *Nano Lett.* **2018**, *18*, 3335.
[43] R. Verre, D. G. Baranov, B Munkhbat, J. Cuadra, M. Käll, T. Shegai, *Nat. Nanotechnol.* **2019**, *14*, 679.
[44] M. Amani, P. Taheri, R. Addou, G. H. Ahn, D. Kiriya, D.-H. Lien, J. W. Ager, R. M. Wallace, A. Javey, *Nano Lett.* **2016**, *16*, 2786.
[45] Y. L. Li, A. Chernikov, X. Zhang, A. Rigosi, H. M. Hill, A. M. van der Zande, D. A. Chenet, E.-M. Shih, J. Hone, T. F. Heinz, *Phys. Rev. B* **2014**, *90*, 205422.
[46] X. Z. Liu, T. Galfsky, Z. Sun, F. N. Xia, E.-C Lin, Y.-H. Lee, S. Kéna-Cohen, V. M. Menon, *Nat. Photonics* **2015**, *9*, 30.
[47] A. Bisht, J. Cuadra, M. Wersäll, A. Canales, T. J. Antosiewicz, T. Shegai, *Nano Lett.* **2019**, *19*, 189.
[48] W. J. Liu, B. Lee, C. H. Naylor, H.-S. Ee, J. Park, A. T. C. Johnson, R. Agarwal, *Nano Lett.* **2017**, *17*, 4541.
[49] P. A. D. Gonçalves, L. Bertelsen, S. S. Xiao, N. A. Mortensen, *Phys. Rev. B* **2018**, *97*, 041402.
[50] M.-E. Kleemann, R. Chikkaraddy, E. M. Alexeev, D. Kos, C. Carnegie, W. Deacon, A. C. de Pury, C. Große, B. de Nijs, J. Mertens, I. T. Alexander, J. B. Jeremy, *Nat. Commun.* **2017**, *8*, 1296.
[51] J. D. Chen, J. Xiang, S. Jiang, Q. F. Dai, S. L. Tie, S. Lan, *Nanoscale* **2018**, *10*, 9153.
[52] J. Xiang, J. D. Chen, S. Jiang, M. C. Panmai, P. L. Li, Y. Xu, Q. F. Dai, S. L. Tie, S. Lan, *Laser & Photonics Rev.* **2019**, *13*, 1800214.
[53] E. del Corro, A. Botello-Méndez, Y. Gillet, A. L. Elias, H. Terrones, S. Feng, C. Fantini, D. Rhodes, N. Pradhan, L. Balicas, X. Gonze, J.-C. Charlier, M. Terrones, M. A. Pimenta, *Nano Lett.* **2016**, *16*, 2363.
[54] B. R. Carvalho, Y. X. Wang, S. Mignuzzi, D. Roy, M. Terrones, C. Fantini, V. H. Crespi, L. M. Malard, M. A. Pimenta, *Nat. Commun.* **2017**, *8*, 14670.
[55] C. X. Cong, J. Z. Shang, X. Wu, B. C. Cao, N. Peimyoo, C. Y. Qiu, L. T. Sun, T. Yu, *Adv. Opt. Mater.* **2014**, *2*, 131.
[56] A. Krasnok, S. Lepeshov, A. Alù, *Opt. Express* **2018**, *26*, 15972.
[57] D. Ovchinnikov, A. Allain, Y.-S. Huang, D. Dumcenco, A. Kis, *ACS Nano* **2014**, *8*, 8174.
[58] H. R. Gutiérrez, N. Perea-López, A. L. Elías, A. Berkdemir, B. Wang, R. T. Lv, F. López-Urías, V. H. Crespi, H. Terrones, M. Terrones, *Nano Lett.* **2012**, *3*, 3447.
[59] M. W. Knight, T. Coenen, Y. Yang, B. J. Brenny, M. Lo-surdo, A. S. Brown, H. O. Everitt, A. Polman, *ACS Nano* **2016**, *9*, 2049.
[60] P. B. Johnson, R. W. Christ, *Phys. Rev. B* **1972**, *6*, 4370.
[61] Y. Gutierrez, D. Ortiz, J. M. Sanz, J. M. Saiz, F. Gonzalez, H. O. Everitt, F. Moreno, *Opt. Express* **2016**, *24*, 20621.